

SCIENTIFIC REPORTS

OPEN

Digital Etch Technique for Forming Ultra-Scaled Germanium-Tin ($\text{Ge}_{1-x}\text{Sn}_x$) Fin Structure

Wei Wang¹, Dian Lei¹, Yuan Dong¹, Xiao Gong¹, Eng Soon Tok² & Yee-Chia Yeo¹ 

We developed a new digital etch process that allows precise etching of Germanium or Germanium-tin ($\text{Ge}_{1-x}\text{Sn}_x$) materials. The digital etch approach consists of $\text{Ge}_{1-x}\text{Sn}_x$ oxide formation by plasma oxidation and oxide removal in diluted hydrochloric acid at room temperature. The first step is a self-limiting process, as the thickness of oxide layer grows logarithmically with the oxidation time and saturates fast. Consistent etch rates in each cycle were found on the $\text{Ge}_{1-x}\text{Sn}_x$ samples, with the surfaces remaining smooth after etch. The digital etch process parameters were tuned to achieve various etch rates. By reducing the radio frequency power to 70W, etch rate of sub-1.2 nm was obtained on a $\text{Ge}_{0.875}\text{Sn}_{0.125}$ sample. The digital etch process was employed to fabricate the $\text{Ge}_{1-x}\text{Sn}_x$ fin structures. Extremely scaled $\text{Ge}_{0.95}\text{Sn}_{0.05}$ fins with 5 nm fin width were realized. The side walls of the $\text{Ge}_{0.95}\text{Sn}_{0.05}$ fins are smooth, and no crystal damage can be observed. This technique provides an option to realize aggressively scaled nanostructure devices based on $\text{Ge}_{1-x}\text{Sn}_x$ materials with high-precision control.

Germanium-tin $\text{Ge}_{1-x}\text{Sn}_x$ has attracted significant research interest due to its potential applications in high-channel mobility metal-oxide-semiconductor field-effect transistors (MOSFETs)^{1–4} and silicon-based infrared photonic devices, e.g. near- and mid-infrared photodetectors^{5–8}. In particular, recent theoretical and experimental studies indicate that strain-free $\text{Ge}_{1-x}\text{Sn}_x$ becomes a direct bandgap material at a Sn composition of about 6.5% to 11%^{9–11}, making it a possible candidate as a gain medium in lasers based on group IV materials^{12,13}. Lasing of a direct bandgap $\text{Ge}_{0.874}\text{Sn}_{0.126}$ grown on Si substrates was reported recently^{14,15}.

Despite the large lattice mismatch between Ge and Sn (~15%) and the low equilibrium solid solubility of Sn in Ge (less than 1%), $\text{Ge}_{1-x}\text{Sn}_x$ with x up to 0.34 can be realized using non-equilibrium growth techniques such as molecular beam epitaxy (MBE) and chemical vapor deposition (CVD)^{16–21}. As a group IV material, $\text{Ge}_{1-x}\text{Sn}_x$ can be integrated with Si-based complementary MOS (CMOS) technology. Bulk $\text{Ge}_{1-x}\text{Sn}_x$ n- and p- MOSFETs were reported recently with CMOS compatible processes^{1–4}.

Ultra-scaled device architectures employing thin-body planar, nanowire or fin-type channels may be used in future CMOS transistors. A Fin-type field-effect transistor (FinFET) may employ $\text{Ge}_{1-x}\text{Sn}_x$ as a high mobility channel material, and methods to form $\text{Ge}_{1-x}\text{Sn}_x$ fins would be required. Formation of $\text{Ge}_{1-x}\text{Sn}_x$ nanostructures using conventional etches is often difficult as vertical or horizontal etch rates lack controllability in the absence of a stopping mechanism. To realize ultra-scaled $\text{Ge}_{1-x}\text{Sn}_x$ devices, a method to precisely etch Ge or $\text{Ge}_{1-x}\text{Sn}_x$ is highly desirable.

Digital etch is a high-precision etch technique that can provide tight control of etch variability. It has been studied for over 25 years on various materials, such as Si, Ge, III-Vs and some oxides^{22–32}. There is a recent increase in interest in digital etch capabilities³³. For Si and Ge, atomic layer etch has been demonstrated using either chlorine Cl or fluorine F adsorption that is subsequently followed by the removal of the halides by Ar ion bombardment^{22–25}. For III-Vs, digital etch with etch rate of 1–3 nm/cycle has been reported using combinations of oxidation and oxide removal processes^{26–29}. Recently, a two-step digital etch process consisting of a fluorine-based plasma etch followed by an acid wet etch was proposed to etch $\text{Ge}_{1-x}\text{Sn}_x$ ³⁴. The formation of tin fluoride SnF_2 inhibits further reactions between $\text{Ge}_{0.922}\text{Sn}_{0.078}$ and F radicals³⁵. However, it is not an ideal self-limiting process due to the physical sputtering of the surface layer. The etch rate varies with plasma etch duration (1.5 nm/cycle

¹Department of Electrical and Computer Engineering, National University of Singapore, 117576, Singapore, Singapore. ²Department of Physics, National University of Singapore, 117551, Singapore, Singapore. Correspondence and requests for materials should be addressed to W.W. (email: elewwei@nus.edu.sg) or Y.-C.Y. (email: yeo@ieee.org)

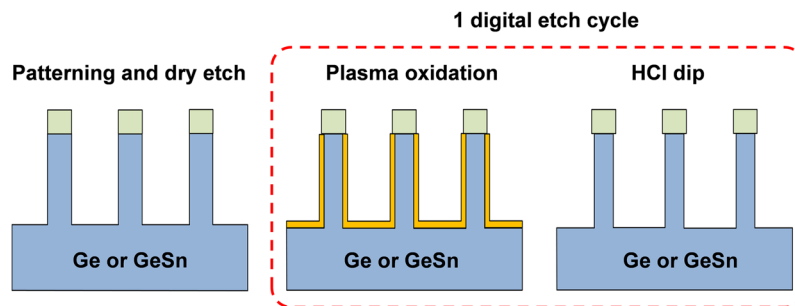


Figure 1. Illustration of the process flow for fabrication of extremely scaled Ge or $\text{Ge}_{1-x}\text{Sn}_x$ fins.

and 3.2 nm/cycle for 10 s and 60 s etch duration, respectively)³⁴. In addition, the formation of SnF_4 is dependent on the initial Sn content, which limits its application for $\text{Ge}_{1-x}\text{Sn}_x$ with low Sn content.

Here we present a new digital etch process that allows the etching of Ge or $\text{Ge}_{1-x}\text{Sn}_x$ structures with sub-1.2 nm precision. The digital etch process is realized at room temperature, which avoids the Sn surface segregation or precipitation. The $\text{Ge}_{1-x}\text{Sn}_x$ surface after digital etch is smooth, and it can be used directly for extremely scaled $\text{Ge}_{1-x}\text{Sn}_x$ fin formation in Ge or $\text{Ge}_{1-x}\text{Sn}_x$ CMOS applications. In addition, such a unique process capability can also enable fabrication of $\text{Ge}_{1-x}\text{Sn}_x$ based nanostructures for a range of Si-compatible photonics and microelectro-mechanical (MEMS) device applications.

The $\text{Ge}_{1-x}\text{Sn}_x$ samples used for this study were grown on 4-inch Ge(100) substrates by a solid-source MBE system. The Ge substrates were cleaned by diluted hydrofluoric acid (DHF) before being loaded into the load-lock chamber of the MBE system. After transferring the substrates into the growth chamber, annealing was performed at 630 °C for 5 minutes to remove the native oxide. The substrate temperature was then adjusted to 100–150 °C for $\text{Ge}_{1-x}\text{Sn}_x$ growth. The thicknesses of the $\text{Ge}_{1-x}\text{Sn}_x$ layers are kept below 50 nm, so that all the $\text{Ge}_{1-x}\text{Sn}_x$ films are fully strained to the Ge substrates²⁰. In addition, a commercial GeOI wafer was used to extract the etch rate of Ge.

To avoid the problem caused by thermal instability of $\text{Ge}_{1-x}\text{Sn}_x$ layer having a high Sn content^{36–38}, a low temperature process is preferred. Our digital etch approach forms a $\text{Ge}_{1-x}\text{Sn}_x$ oxide through exposure to oxygen plasma in an ashers, and removes the oxide in dilute hydrochloric acid HCl (10%) for 30 s at room temperature. The plasma oxidation was performed at a pressure of 300 mTorr. As the oxidation reaction (first step) is self-limiting, the etch depth is no longer dependent on the etch time, but is dependent on the number of etching cycles. By repeating these two steps, the extremely scaled Ge or $\text{Ge}_{1-x}\text{Sn}_x$ fins can be formed in a controlled manner as shown schematically in Fig. 1.

$\text{Ge}_{1-x}\text{Sn}_x$ Oxide Formation by Low Temperature Plasma Oxidation

It was reported that migration of Sn atoms from the $\text{Ge}_{1-x}\text{Sn}_x$ surface and from inside the $\text{Ge}_{1-x}\text{Sn}_x$ to the $\text{Ge}_{1-x}\text{Sn}_x$ oxide occurs during thermal oxidation³⁹. Instead of using a conventional thermally activated oxidation at high temperature, a plasma activated oxidation is used as it can be done at low temperature. To better understand the mechanism of the digital etch process on $\text{Ge}_{1-x}\text{Sn}_x$, X-ray photoelectron spectroscopy (XPS) was performed to investigate the formation of $\text{Ge}_{1-x}\text{Sn}_x$ oxide during plasma oxidation, and removal of the surface oxide in HCl solution.

Figure 2a and b show the Ge 2p_{3/2} and Sn 3d photoelectron core spectra of the $\text{Ge}_{0.875}\text{Sn}_{0.125}/\text{Ge}$ sample after plasma oxidation, with radio frequency (RF) power of 250 W and plasma oxidation time of 120 s. Both the peaks of the Ge and Sn oxides can be observed in the Ge 2p_{3/2} and Sn 3d photoelectron spectra, respectively. The binding energies (BEs) of these peaks agree well with the reported values of BEs for stoichiometric GeO_2 and SnO_2 ^{39,40}. As Ge 2p_{3/2} photoelectrons have a short inelastic mean free path λ (λ for Ge 2p_{3/2} is ~ 9.7 Å)⁴¹, no Ge peak can be observed in Fig. 2a, while clear Sn peaks can be identified in Fig. 2b. The core-level spectra were fitted using a combination of Gaussian and Lorentzian line shapes, together with a Shirley-typed background subtraction. This results in the overall blue line fitting of the core-level spectra with their respective peak components (gray lines). The Sn content in the $\text{Ge}_{1-x}\text{Sn}_x$ oxide layer can be calculated using $A_{\text{Sn-O}}/(A_{\text{Sn-O}} + A_{\text{Ge-O}})$, where $A_{\text{Sn-O}}$ and $A_{\text{Ge-O}}$ are the normalized areas of the Sn-oxide and Ge-oxide peaks, respectively. We found that the Sn content x in the $\text{Ge}_{1-x}\text{Sn}_x$ oxide layer is 13.8%.

Figure 2c and d show the Ge 2p_{3/2} and Sn 3d spectra of the $\text{Ge}_{0.875}\text{Sn}_{0.125}/\text{Ge}$ sample after plasma oxidation and HCl dipping. There were no obvious peaks related to Ge or Sn oxides in the Ge 2p_{3/2} and Sn 3d spectra, indicating that the $\text{Ge}_{1-x}\text{Sn}_x$ oxide formed by oxygen plasma can be effectively dissolved using a wet chemical treatment with dilute HCl solution. In Fig. 2c, a small shoulder can be observed besides Ge peak, which indicates a minor BE peak at 1218.9 eV after fitting. The peak is associated with native oxide on the $\text{Ge}_{1-x}\text{Sn}_x$ layer surface formed from atmospheric exposure before the *ex situ* XPS measurement. The smaller BE of the observed Ge oxide peak compared with that of stoichiometric GeO_2 indicates suboxide GeO_x formation on the $\text{Ge}_{1-x}\text{Sn}_x$ layer owing to atmospheric exposure. The BEs of Sn 3d peaks slightly increases after HCl dip, which is attributed to the band bending originating from different charged states at the GeSn oxide/ GeSn interfaces⁴². The Sn content in the surface $\text{Ge}_{1-x}\text{Sn}_x$ region was calculated to be 12.0% using the normalized areas of the Sn and Ge peaks (Fig. 2c,d), which is close to that in bulk region, and slightly smaller than that in the $\text{Ge}_{1-x}\text{Sn}_x$ oxide layer formed by plasma oxidation. This result indicates negligible Sn atoms migration from inside the $\text{Ge}_{1-x}\text{Sn}_x$ to surface occurs during the plasma oxidation at room temperature.

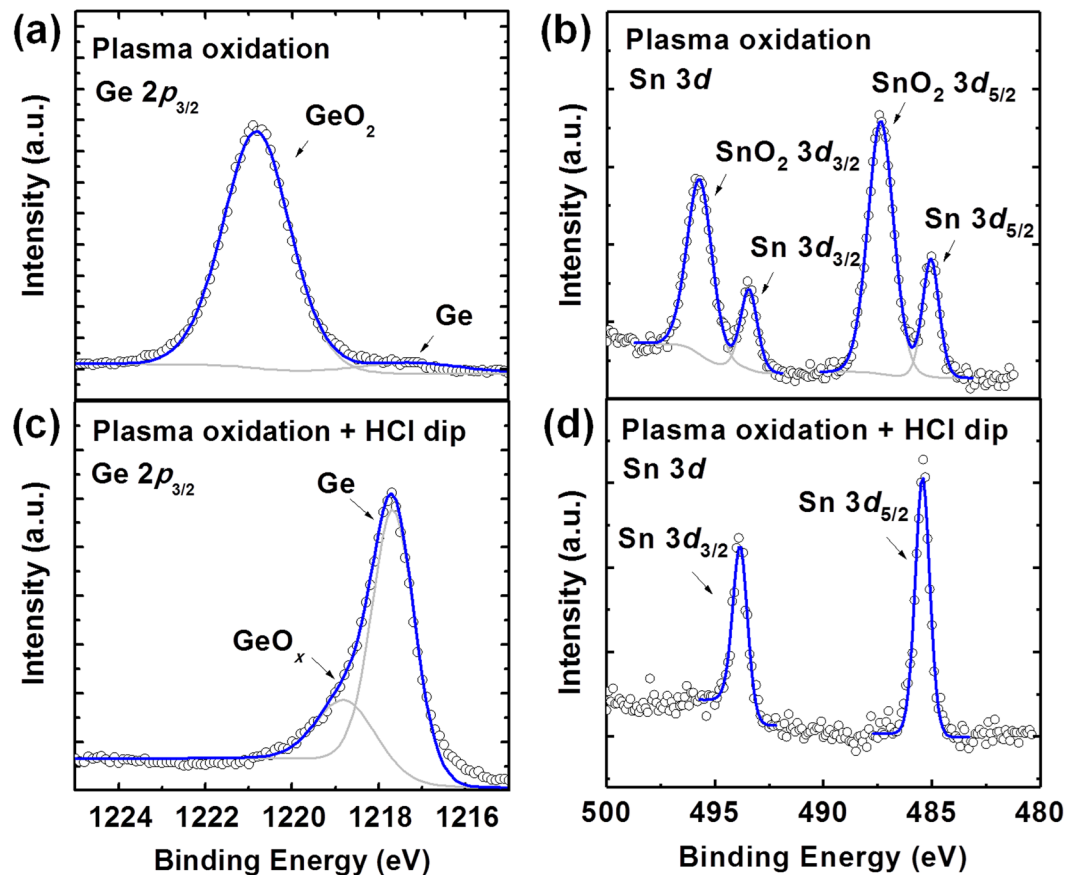


Figure 2. (a) Ge $2p_{3/2}$ and (b) Sn $3d$ XPS spectra of $\text{Ge}_{0.875}\text{Sn}_{0.125}/\text{Ge}(001)$ sample after plasma oxidation. (c) Ge $2p_{3/2}$ and (d) Sn $3d$ XPS spectra of oxidized $\text{Ge}_{0.875}\text{Sn}_{0.125}/\text{Ge}(001)$ sample after HCl dipping. XPS results indicate the oxide formation and removal in one digital etch cycle.

Digital Etch of Ge and $\text{Ge}_{1-x}\text{Sn}_x$ layers. High-resolution X-ray diffraction (HRXRD) was used to investigate the Sn content and crystallinity of the $\text{Ge}_{1-x}\text{Sn}_x$ samples. Figure 3a shows the HRXRD scans around the 004 diffraction point for the $\text{Ge}_{0.875}\text{Sn}_{0.125}/\text{Ge}$ samples before and after digital etch. Clear GeSn and Ge peaks can be identified for the as-grown $\text{Ge}_{0.875}\text{Sn}_{0.125}$ sample, and the presence of interference fringes surrounding the GeSn peak suggests good interface quality. The full width at half maximum (FWHM) of the GeSn diffraction peak increases with increasing etch cycles, which indicates the decrease of $\text{Ge}_{0.875}\text{Sn}_{0.125}$ layer thickness according to Scherrer's formula⁴³. This is consistent with the increasing interval of the interference fringes after digital etch. After an 8-cycle digital etch, the GeSn peak moves slightly towards the Ge peak. The Sn content can be calculated to be 11.7%, which corresponds to a Sn content decrease of approximately 0.8%.

On the other hand, X-ray reflectivity (XRR) measurements have been performed on the $\text{Ge}_{1-x}\text{Sn}_x$ samples before and after digital etch. XRR can be used to determine thickness of thin film with high accuracy by analysing X-ray reflection intensity curves from grazing incident X-ray beam. As a non-destructive technique, no additional lithographic patterning is needed for etch depth calibration. Figure 3b shows the experimental (open black circle) and simulated (blue curve) XRR curves of the as-grown $\text{Ge}_{0.875}\text{Sn}_{0.125}$, the $\text{Ge}_{0.875}\text{Sn}_{0.125}$ after plasma oxidation, and the $\text{Ge}_{0.875}\text{Sn}_{0.125}$ after HCl dipping. The thickness of the as-grown $\text{Ge}_{0.875}\text{Sn}_{0.125}$ film is 30.7 ± 0.2 nm, which can be obtained by fitting the reflected X-ray intensity versus incident angle. The thickness of the $\text{Ge}_{0.875}\text{Sn}_{0.125}$ film decreases with increasing number of digital etch cycles. After a 4-cycle digital etch and plasma oxidation, the thickness of $\text{Ge}_{0.875}\text{Sn}_{0.125}$ film drops to 19.4 ± 0.2 nm. The etch rate can be estimated to be 2.2 nm/cycle. In addition, the thickness of $\text{Ge}_{1-x}\text{Sn}_x$ oxide formed by plasma oxidation can be also extracted by XRR, which is 3.9 ± 0.2 nm. Based on the molar mass and density of Ge and GeO_2 , for every 2.2 nm-thick Ge consumed, 3.97 nm-thick GeO_2 will appear. This is consistent with the XRR results.

Figure 4a shows the etched layer thickness as a function of etch cycle number for $\text{Ge}_{1-x}\text{Sn}_x$ samples with various Sn content. The RF power is fixed at 250 W, and the plasma oxidation time is fixed at 120 s. The etched thickness for the $\text{Ge}_{1-x}\text{Sn}_x$ samples was extracted from XRR, while that for the GeOI was obtained from ellipsometry measurements. Good linear fits can be observed in all the samples, which confirm that a consistent depth of Ge or $\text{Ge}_{1-x}\text{Sn}_x$ is etched away each cycle. The etch rate extracted from the slope is ~ 2.2 , ~ 1.9 , and ~ 1.4 nm/cycle for the $\text{Ge}_{0.875}\text{Sn}_{0.125}$, $\text{Ge}_{0.95}\text{Sn}_{0.05}$, and Ge, respectively (Fig. 4b). It was reported that SiGe alloys had higher oxidation rates than Si under thermal oxidation conditions^{44,45}. This enhancement under thermal oxidation increases with increasing initial Ge concentration in the alloy. Therefore, it could be explained in terms of the Si–Ge bond being weaker than the Si–Si bond. Similarly, the presence of Sn atoms results in weaker Ge–Sn bonds than Ge–Ge

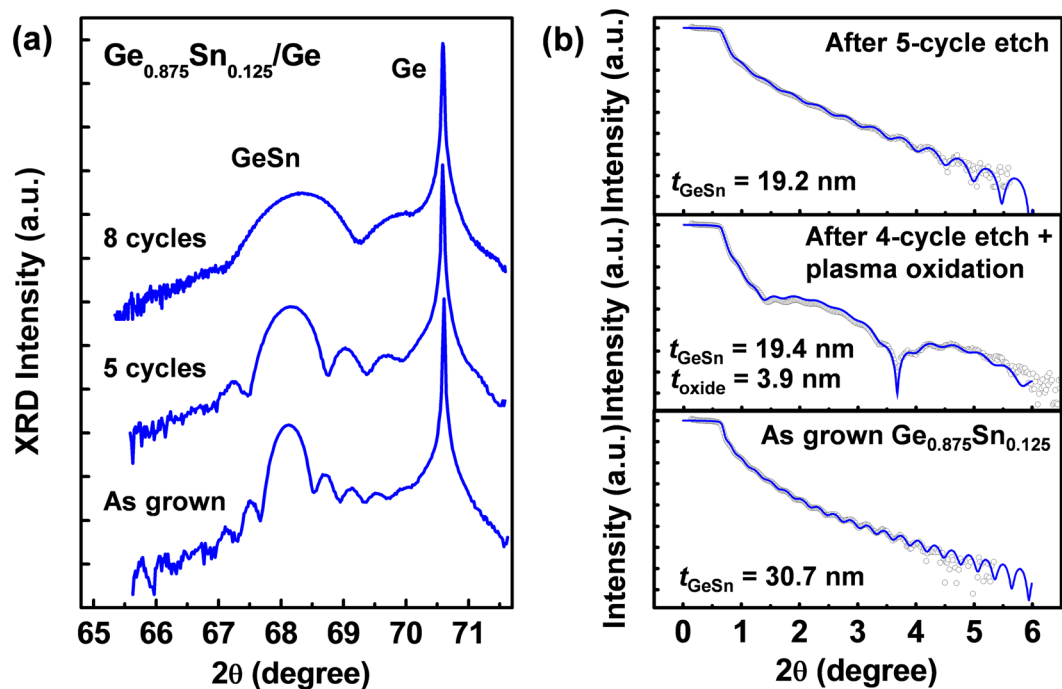


Figure 3. (a) (004) HRXRD curves of the as-grown $\text{Ge}_{0.875}\text{Sn}_{0.125}$, and the sample after 5-cycle and 8-cycle digital etch. (b) Experimental and simulated XRR curves of the as-grown $\text{Ge}_{0.875}\text{Sn}_{0.125}$, and the sample after 5-cycle plasma oxidation and HCl etch.

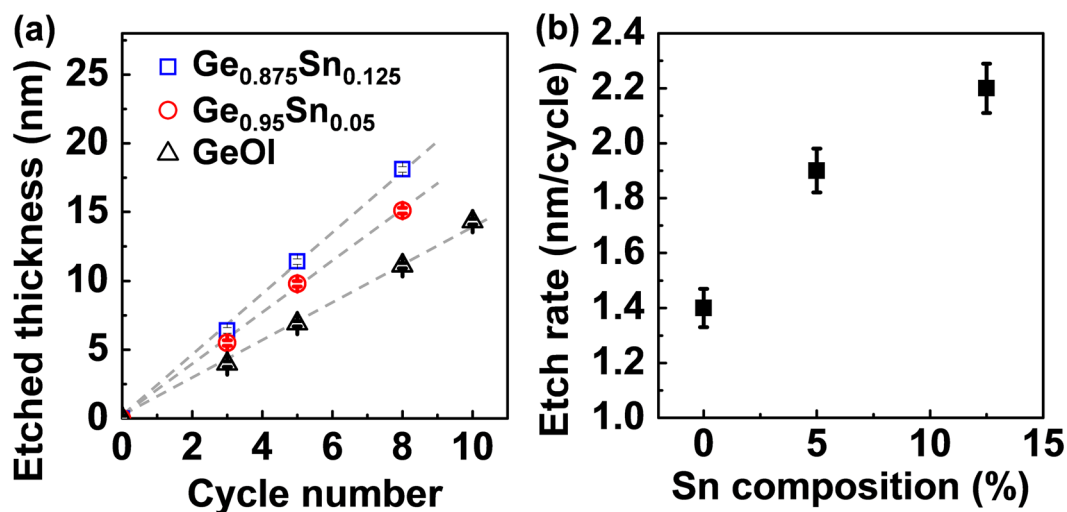


Figure 4. (a) Etched thickness versus cycle number with various Sn contents and (b) the extracted etch rate. Consistent depth of Ge or $\text{Ge}_{1-x}\text{Sn}_x$ is etched away each cycle.

bond, and weaker still Sn-Sn bonds at the sample surface (at $T = 298$ K, the dissociation energies for the Ge-Ge, Ge-Sn, and Sn-Sn bonds are 264.4 ± 6.8 , 230.1 ± 13 , and 187.1 ± 0.3 kJ/mol, respectively)⁴⁶, which may lead to the increased oxidation rate (etch rate) with increasing Sn content. In addition, the introducing Sn may slightly degrade the residual order in the oxide layer, which also affect the etch rate.

Surface area to volume ratio increases with downscaling of device dimensions and surface properties can appreciably affect device electronic properties. Atomic force microscope (AFM) was employed to investigate the surface roughness of the Ge or $\text{Ge}_{1-x}\text{Sn}_x$ samples after digital etch. Figure 5a–c show the AFM images for the as-grown $\text{Ge}_{0.875}\text{Sn}_{0.125}$ sample, and the $\text{Ge}_{0.875}\text{Sn}_{0.125}$ samples after 5-cycle and 8-cycle digital etch, respectively. The scan size is $10 \times 10 \mu\text{m}^2$, and the z-axis display range of all the images is set to be -0.8 to 0.8 nm, as illustrated on the left side of the figure. The surface remains smooth with ~ 18 nm-thick $\text{Ge}_{0.875}\text{Sn}_{0.125}$ etched away after 8-cycle digital etch, with the root mean square (RMS) roughness increasing slightly from 0.24 to 0.32 nm. Figure 5d and e show the AFM images of the commercial GeOI wafer and the wafer after 10-cycle digital etch. It

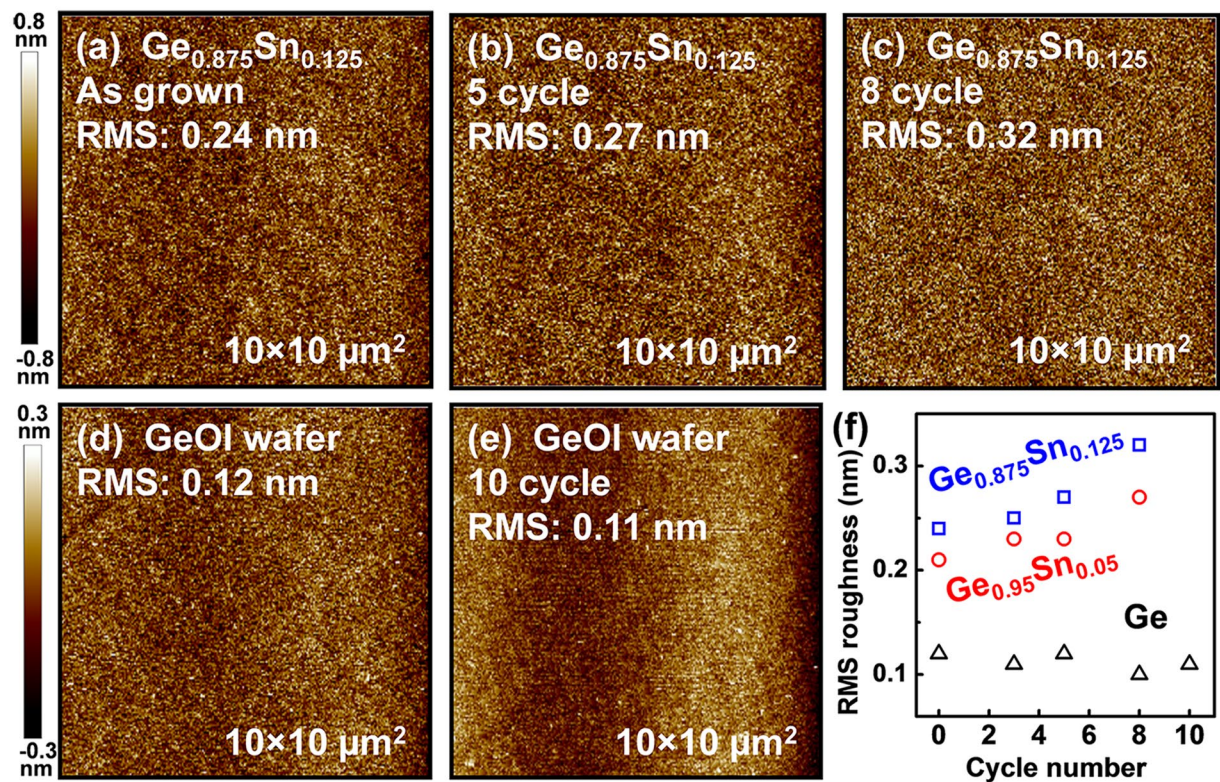


Figure 5. AFM images of (a) the as grown $\text{Ge}_{0.875}\text{Sn}_{0.125}$, and the sample after (b) 5 cycle and (c) 8 cycle digital etch. AFM images of (d) the GeOI sample, and the sample after (e) 11 cycle digital etch. (f) Surface RMS roughness evolution with cycle number. The $\text{Ge}_{1-x}\text{Sn}_x$ surface remains smooth after digital etch.

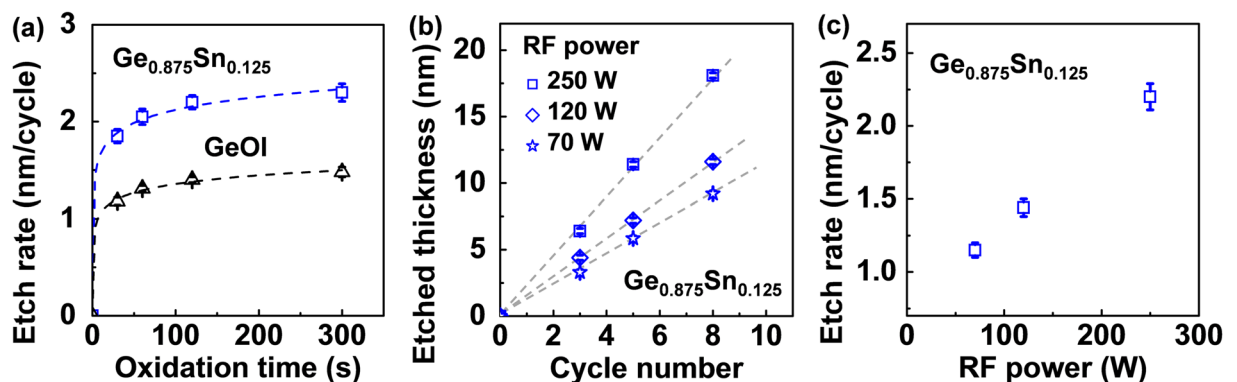


Figure 6. (a) Etch rate as a function of oxidation time for Ge and $\text{Ge}_{0.875}\text{Sn}_{0.125}$. The oxide layer thickness grows logarithmically with the oxidation time and saturates fast. (b) Etched thickness versus cycle number under different RF power and (c) extracted etch rate. The etch rate decreases with decreasing RF power.

was found that the RMS roughness of GeOI samples after etch remains as small as ~ 0.11 nm. Figure 5f summarizes the RMS roughness of Ge and $\text{Ge}_{1-x}\text{Sn}_x$ samples after various digital etch cycles. The digital etch increases the RMS roughness slightly for $\text{Ge}_{1-x}\text{Sn}_x$ samples but not for GeOI samples. Both GeO_2 and SnO_2 were formed on $\text{Ge}_{1-x}\text{Sn}_x$ samples during plasma oxidation. The slightly increased RMS roughness after successive etching cycles may be related to the residual SnO_2 after HCl dip in which SnO_2 masks subsequent oxidation, or related to the different oxidation rates for Ge and Sn.

Figure 6a shows the measured Ge and $\text{Ge}_{0.875}\text{Sn}_{0.125}$ digital etch rates as a function of plasma oxygen exposure time. The RF power is fixed at 250 W. It is noted that for both the Ge and $\text{Ge}_{0.875}\text{Sn}_{0.125}$ samples, the etch rate increases rapidly for the first 120 s of oxidation time, and then saturates fast to an etch rate of ~ 1.4 and ~ 2.2 nm/cycle, respectively. Deal and Grove proposed that the thermal oxidation rate could be determined by a combination of two processes⁴⁷. One is the actual chemical reaction of oxygen O at the interface, and the other is the diffusion of oxygen through the previously formed oxide film. The combination of these processes resulted in

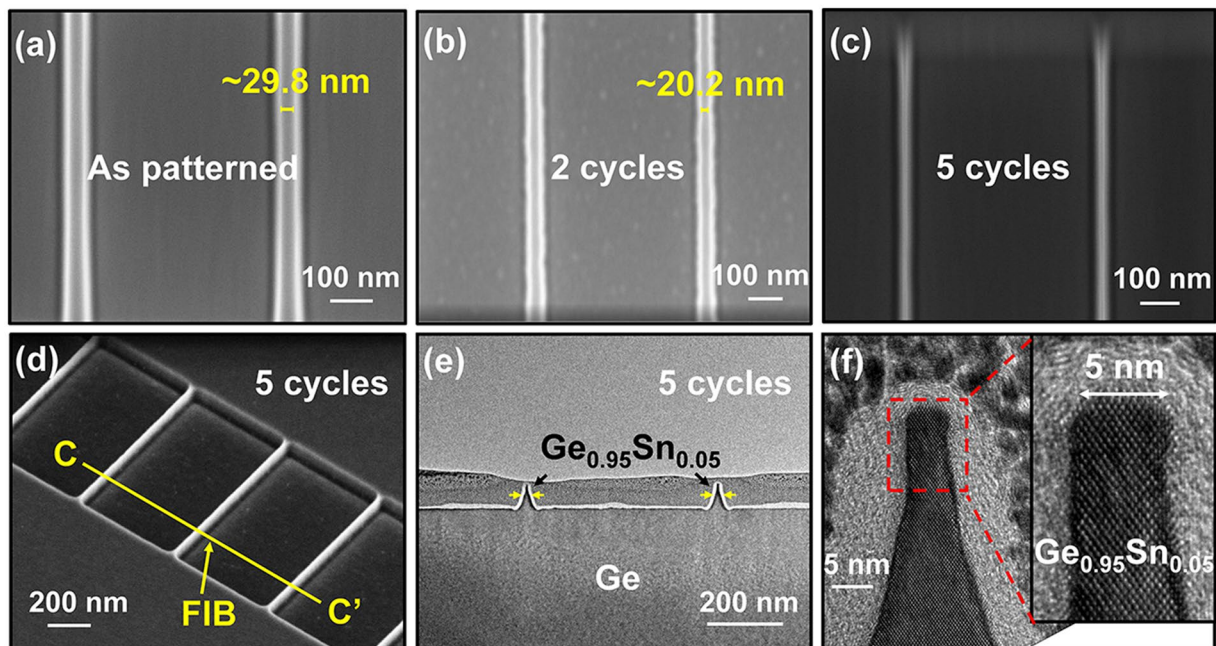


Figure 7. Top view SEM images of (a) the $\text{Ge}_{0.95}\text{Sn}_{0.05}$ fins formation by EBL and Cl-based dry etch, and the $\text{Ge}_{0.95}\text{Sn}_{0.05}$ fins after (b) 2-cycle and (c) 5-cycle digital etch. (d) Tilt view SEM image of the $\text{Ge}_{0.95}\text{Sn}_{0.05}$ fins after 5-cycle digital etch. (e) XTEM and (f) HRTEM images demonstrate high crystalline quality $\text{Ge}_{0.95}\text{Sn}_{0.05}$ fins with fin width of ~ 5 nm.

the linear-parabolic relationship between the oxide thickness and the oxidation time. However, the Deal-Grove model could not explain the plasma oxidation kinetics well due to the extracted negative value of the reaction rate^{48,49}. K. Kim *et al.* proposed a complementary model of the Deal-Grove oxidation theory to explain the plasma oxidation kinetics, which is involved with the atomic diffusion of O atoms⁴⁹. They found that the oxide layer thickness y grows logarithmically with increasing oxidation time t as shown below:

$$y = \frac{A}{2} \ln \left(\frac{2B(t + \tau)}{A^2} + 1 \right), \quad (1)$$

where A and B are the parameters related to the effective diffusion coefficient of O atoms in the oxide, and the concentration of O atoms at the oxide surface and in the oxide layer; τ is the oxidation time for native oxide formation. This logarithmic limit shows faster saturation of the diffusion-limited process compared with the parabolic limit from the Deal-Grove model. Simply assuming $\tau = 0$, good experimental fits for the etch rate (oxide thickness) were obtained with this theory, as shown in Fig. 6a (dash line).

To achieve digital etch with higher precision, the etch rate should be reduced. As discussed, the etch rate can be tuned by varying the oxidation time. However, an ideal digital etch should eliminate the requirement for timed etching, and decreasing oxidation time may lead to larger variation of etch rate. The etch rate can be also tuned by varying the RF power or gas pressure. Figure 6b shows the etched thickness of $\text{Ge}_{0.875}\text{Sn}_{0.125}$ as a function of etch cycle, and the etch rates were extracted in Fig. 6c. The oxidation time is fixed at 120 s. The etch rate decreases with decreasing RF power, and etch rate of sub-1.2 nm/cycle was obtained with the RF power reduced to 70 W. The main oxidizing species should be atomic oxygen during plasma oxidation⁴⁹. As the atomic oxygen concentration increases with higher RF power, the etch rate increases with higher RF power^{49,50}.

Formation of Extremely Scaled $\text{Ge}_{1-x}\text{Sn}_x$ Fins. Digital etch technique provides high-precision control of etch, and can be used to realize extremely scale devices, such as deeply scaled FinFETs. According to the 2013 International Technology Roadmap for Semiconductors (ITRS) Overall Roadmap Technology Characteristics (ORTC)⁵¹, sub-5 nm fin width is required in the sub-10 nm technology nodes. Here we explore the possibility of realizing $\text{Ge}_{1-x}\text{Sn}_x$ fins with 5 nm fin width.

The ~ 28 nm-thick $\text{Ge}_{0.95}\text{Sn}_{0.05}/\text{Ge}$ sample was used for forming fins. After electron beam lithography (EBL) patterning and chlorine-based dry etch, a trapezoidal $\text{Ge}_{0.95}\text{Sn}_{0.05}$ fin structure was formed, with fin height of ~ 70 nm and sidewall slope of $\sim 75^\circ$. Details of the $\text{Ge}_{0.95}\text{Sn}_{0.05}$ fins fabrication process are provided in the Methods section. Figure 7a shows the top-view scanning electron microscope (SEM) image of the as-patterned $\text{Ge}_{0.95}\text{Sn}_{0.05}$ fins after dry etch. The fin width is ~ 29.8 nm. Digital etch (RF: 250 W, Oxidation time: 120 s) was performed on the sample, and the fin width obviously shrinks with increased etch cycle (Fig. 7b and c). The etch rate of ~ 2.4 nm/cycle can be extracted from the SEM image, which is higher than that extracted from bulk $\text{Ge}_{0.95}\text{Sn}_{0.05}$ sample. The different etch rate should arise from different crystal orientation of the etch surface. The patterned $\text{Ge}_{0.95}\text{Sn}_{0.05}$

fins are along <110> direction, thus the oxidation and etch occur on the {110} oriented surfaces. Ligenza *et al.* suggested that the orientation effect on oxidation rate might be caused by differences in the dangling bond density on the various crystal surfaces⁵². As the {100} surfaces have lower dangling bond density than {110} surfaces, the oxidation rate or etch rate for {100} surfaces is slower.

Figure 7d shows the tilted-view SEM image of the Ge_{0.95}Sn_{0.05} fins after 5-cycle digital etch. Extremely scaled Ge_{0.95}Sn_{0.05} fins were produced with good uniformity. The region where the transmission electron microscope (TEM) lamella was prepared by focused ion beam (FIB) milling is highlighted by a green solid line along CC'. The cross-sectional TEM image of the Ge_{0.95}Sn_{0.05} fins is shown in Fig. 7e. Trapezoidal fins with narrow upper base were formed. The high resolution TEM (HRTEM) image of one Ge_{0.95}Sn_{0.05} fin is presented in Fig. 7f, demonstrating the high crystalline quality of the Ge_{0.95}Sn_{0.05} fins. The fin width was trimmed down to 5 nm after 5-cycle digital etch. The side wall of Ge_{0.95}Sn_{0.05} fin is smooth with no observed crystal damage as shown in the inset of Fig. 7f.

In summary, we have demonstrated a new digital etch technique for controllable etching of Ge or Ge_{1-x}Sn_x materials with high precision. The two-step digital etch approach consists of Ge_{1-x}Sn_x oxide formation by low temperature plasma oxidation and the oxide removal in diluted HCl. The plasma oxidation is a good self-limiting process, as the oxide layer thickness grows logarithmically with the oxidation time and saturates fast. Consistent etch rate can be obtained on the Ge_{1-x}Sn_x samples, independent of the initial Sn content. After several cycles of digital etch, the surface morphologies and RMS roughness do not show discernible changes as compared to the as-grown samples. Extremely scaled Ge_{0.95}Sn_{0.05} fins with 5 nm fin width were demonstrated with the digital etch technique. The Ge_{0.95}Sn_{0.05} fins show high crystalline quality, with smooth side wall. The unique process capability can facilitate fabrication of Ge or Ge_{1-x}Sn_x based nanostructures with high-precision control for a range of CMOS, Si-compatible photonics and microelectro-mechanical (MEMS) device applications.

Methods

X-ray photoelectron spectroscopy (XPS). Measurements were performed using a VG ESCALAB 220i-XL imaging XPS system. Monochromatic aluminum (Al) K α X-ray (1486.7 eV) was employed with the photoelectrons collected at a take-off angle of 90° (with respect to the sample surface). After Shirley-type background subtraction, the normalized peak area is calculated by taking into consideration of the corresponding Scofield photoionization cross-sections (SF), the transmission function of the spectrometer by the manufacturer (TXFN) and the energy compensation factor. The atomic concentration of Sn, x , is calculated using

$$x = \frac{A_{\text{Sn}}}{A_{\text{Sn}} + A_{\text{Ge}}}, \quad (2)$$

where A_{Sn} is the normalized Sn peak area and A_{Ge} is the normalized Ge peak area.

High-resolution X-ray diffractometry (HRXRD). HRXRD was used to investigate the crystalline quality, composition, and strain of the samples by using the X-ray demonstration and development (XDD) beamline at the Singapore Synchrotron Light Source (SSLS). The wavelength of incident X-ray beam was 0.1634 nm. The diffractometer is the Huber 4-circle system 90000-0216/0, with high-precision 0.0001° step size for omega and two-theta scans. The storage ring, Helios 2, was running at 700 MeV with typical stored electron beam current of 300 mA. X-ray reflectivity measurements were also done at the SSLS.

Tapping mode atomic force microscope (AFM, Bruker Dimension FastScan). AFM was employed to characterize the surface morphology and roughness of the samples before and after digital etch. The background slope was removed by subtracting a first order plane fit, and the tilt was removed by a first order flatten with the NanoScope Analysis software.

Transmission electron microscope (TEM, Tecnai G2 F20 X-Twin). TEM was employed to investigate the extremely scaled Ge_{0.95}Sn_{0.05} fins after digital etch. Specimen for TEM examination was prepared by the Defect Analyzer (DA) 300 Focused Ion Beam (FIB) systems.

Formation of Ge_{0.95}Sn_{0.05} fins. The fins were patterned using a JEOL JBX-6300FS Electron Beam Lithography (EBL) System, with hydrogen silsesquioxane (HSQ) acting as negative tone electron beam resist. The process includes: 1. 2% HSQ spin coat with spin-speed of 3000 rpm; 2. Hot plate bake at 250 °C for 2 minutes; 3. EBL exposure at a base dose of ~8000 $\mu\text{C}/\text{cm}^2$; 4. Photoresist development of 1 minute using NaOH:NaCl:H₂O = 1:4:100 solution. 5. Rinse gently with flowing DI water.

After EBL patterning, chlorine-based dry etch was used to form the fin structure by inductively coupled plasma (ICP). Process parameters include ICP power of 100 W, RF power of 100 W, Cl₂ flow of 50 sccm, pressure of 10 mTorr, and temperature of 25 °C.

References

- Guo, P. & Han, G. *et al.* Ge_{0.97}Sn_{0.03} p-channel metal-oxide-semiconductor field-effect transistors: Impact of Si surface passivation layer thickness and post metal annealing. *J. Appl. Phys.* **114**, 044510, doi:10.1063/1.4816695 (2013).
- Gupta, S. & Gong, X. *et al.* New materials for post-Si computing: Ge and GeSn devices. *MRS Bulletin* **39**, 678–686, doi:10.1557/mrs.2014.163 (2014).
- Gupta, S., Vincent, B. *et al.* GeSn channel nMOSFETs: Material potential and technological outlook. *Symp. VLSI Technol., Dig. Tech.* pp. 95–96 (2012).
- Fang, Y. C. & Chen, K. Y. *et al.* N-MOSFETs Formed on Solid Phase Epitaxially Grown GeSn Film with Passivation by Oxygen Plasma Featuring High Mobility. *ACS Appl. Mater. Interfaces* **7**, 26374–80, doi:10.1021/acsami.5b08518 (2015).
- Soref, R. Mid-infrared photonics in silicon and germanium. *Nat. Photonics* **4**, 495–497, doi:10.1038/nphoton.2010.171 (2010).
- Su, S. & Cheng, B. *et al.* GeSn pin photodetector for all telecommunication bands detection. *Opt. express* **19**, 6400–5, doi:10.1364/OE.19.006400 (2011).

7. Oehme, M. & Kostecki, K. *et al.* GeSn-on-Si normal incidence photodetectors with bandwidths more than 40 GHz. *Opt. express* **22**, 839–46, doi:[10.1364/OE.22.000839](https://doi.org/10.1364/OE.22.000839) (2014).
8. Dong, Y. & Wang, W. *et al.* Germanium-tin on Si avalanche photodiode: device design and technology demonstration. *IEEE Trans. Electron Devices* **62**, 128–135, doi:[10.1109/TED.2014.2366205](https://doi.org/10.1109/TED.2014.2366205) (2015).
9. D'Costa, V. R. & Cook, C. S. *et al.* Optical critical points of thin-film Ge_{1-y}Sn_y alloys: a comparative Ge_{1-y}Sn_y/Ge_{1-x}Si_x study. *Phys. Rev. B* **73**, 125207, doi:[10.1103/PhysRevB.73.125207](https://doi.org/10.1103/PhysRevB.73.125207) (2006).
10. Gallagher, J. D. *et al.* Compositional dependence of the bowing parameter for the direct and indirect band gaps in Ge_{1-y}Sn_y alloys. *Appl. Phys. Lett.* **105**, 142102, doi:[10.1063/1.4897272](https://doi.org/10.1063/1.4897272) (2014).
11. Lin, H. & Chen, R. *et al.* Investigation of the direct band gaps in Ge_{1-x}Sn_x alloys with strain control by photoreflectance spectroscopy. *Appl. Phys. Lett.* **100**, 102109, doi:[10.1063/1.3692735](https://doi.org/10.1063/1.3692735) (2012).
12. Mączko, H. S., Kudrawiec, R. & Gladysiewicz, M. Material gain engineering in GeSn/Ge quantum wells integrated with an Si platform. *Sci. Rep* **6**, 34082, doi:[10.1038/srep34082](https://doi.org/10.1038/srep34082) (2016).
13. Huang, Z. M. *et al.* Emission of direct-gap band in germanium with Ge-GeSn layers on one-dimensional structure. *Sci. Rep* **6**, 24802, doi:[10.1038/srep24802](https://doi.org/10.1038/srep24802) (2016).
14. Wirths, S. & Geiger, R. *et al.* Lasing in direct-bandgap GeSn alloy grown on Si. *Nat. Photonics* **9**, 88–92, doi:[10.1038/nphoton.2014.321](https://doi.org/10.1038/nphoton.2014.321) (2015).
15. Al-Kabi, S. & Ghetmiri, S. A. *et al.* An optically pumped 2.5 μm GeSn laser on Si operating at 110 K. *Appl. Phys. Lett.* **109**, 171105, doi:[10.1063/1.4966141](https://doi.org/10.1063/1.4966141) (2016).
16. He, G. & Atwater, H. A. Synthesis of epitaxial Sn_xGe_{1-x} alloy films by ion-assisted molecular beam epitaxy. *Appl. Phys. Lett.* **68**, 664–666, doi:[10.1063/1.116502](https://doi.org/10.1063/1.116502) (1996).
17. Takeuchi, S. & Sakai, A. *et al.* Growth and structure evaluation of strain-relaxed Ge_{1-x}Sn_x buffer layers grown on various types of substrates. *Semicond. Sci. Technol.* **22**, S231–S235, doi:[10.1088/0268-1242/22/1/S54](https://doi.org/10.1088/0268-1242/22/1/S54) (2007).
18. Kouvetakis, J. & Menendez, J. *et al.* Tin-based group IV semiconductors: New platforms for opto- and microelectronics on silicon. *Annu. Rev. Mater. Res.* **36**, 497–554, doi:[10.1146/annurev.matsci.36.090804.095159](https://doi.org/10.1146/annurev.matsci.36.090804.095159) (2006).
19. Bhargava, N. & Coppinger, M. *et al.* Lattice constant and substitutional composition of GeSn alloys grown by molecular beam epitaxy. *Appl. Phys. Lett.* **103**, 041908, doi:[10.1063/1.4816660](https://doi.org/10.1063/1.4816660) (2013).
20. Vincent, B. & Gencarelli, F. *et al.* Undoped and *in-situ* B doped GeSn epitaxial growth on Ge by atmospheric pressure-chemical vapor deposition. *Appl. Phys. Lett.* **99**, 152103, doi:[10.1063/1.3645620](https://doi.org/10.1063/1.3645620) (2011).
21. Wang, W. & Zhou, Q. *et al.* Critical thickness for strain relaxation of Ge_{1-x}Sn_x (x ≤ 0.17) grown by molecular beam epitaxy on Ge (001). *Appl. Phys. Lett.* **106**, 232106, doi:[10.1063/1.4922529](https://doi.org/10.1063/1.4922529) (2015).
22. Matsuura, T. & Murota, J. *et al.* Self-limited layer-by-layer etching of Si by alternated chlorine adsorption and Ar⁺ ion irradiation. *Appl. Phys. Lett.* **63**, 2803–2805, doi:[10.1063/1.110340](https://doi.org/10.1063/1.110340) (1993).
23. Athavale, S. D. & Economou, D. J. Realization of atomic layer etching of silicon. *J. Vac. Sci., Technol. B* **14**, 3702, doi:[10.1116/1.588651](https://doi.org/10.1116/1.588651) (1996).
24. Ikeda, K. *et al.* Atomic layer etching of germanium. *Appl. Surf. Sci.* **112**, 87–91, doi:[10.1016/S0169-4332\(96\)00995-6](https://doi.org/10.1016/S0169-4332(96)00995-6) (1997).
25. Sugiyama, T. *et al.* Atomic-layer etching of Ge using an ultraclean ECR plasma. *Appl. Surf. Sci.* **112**, 187–190, doi:[10.1016/S0169-4332\(96\)01026-4](https://doi.org/10.1016/S0169-4332(96)01026-4) (1997).
26. DeSalvo, G. C. & Bozada, C. A. *et al.* Wet chemical digital etching of GaAs at room temperature. *J. Electrochem. Soc.* **143**, 3652, doi:[10.1149/1.1837266](https://doi.org/10.1149/1.1837266) (1996).
27. Hennessy, K. & Badolato, A. *et al.* Tuning photonic crystal nanocavity modes by wet chemical digital etching. *Appl. Phys. Lett.* **87**, 021108, doi:[10.1063/1.1992656](https://doi.org/10.1063/1.1992656) (2005).
28. Lee, S., Huang, C. Y. *et al.* III–V/Ge channel MOS device technologies in nano CMOS era. 2013 *Symp. VLSI Technol.*, Dig. Tech. Pap. 246–247 (2013).
29. Lin, J. & Zhao, X. *et al.* A novel digital etch technique for deeply scaled III–V MOSFETs. *IEEE Electron Device Lett* **35**, 440–442, doi:[10.1109/LED.2014.2305668](https://doi.org/10.1109/LED.2014.2305668) (2014).
30. Rauf, S. & Sparks, T. *et al.* A molecular dynamics investigation of fluorocarbon based layer-by-layer etching of silicon and SiO₂. *J. Appl. Phys.* **101**, 033308, doi:[10.1063/1.2464192](https://doi.org/10.1063/1.2464192) (2007).
31. Park, J. B. *et al.* Atomic layer etching of ultra-thin HfO₂ film for gate oxide in MOSFET devices. *J. Phys. D: Appl. Phys* **42**, 055202, doi:[10.1088/0022-3727/42/5/055202](https://doi.org/10.1088/0022-3727/42/5/055202) (2009).
32. Lee, Y. & George, S. M. Atomic Layer Etching of Al₂O₃ Using Sequential, Self-Limiting Thermal Reactions with Sn (acac)₂ and Hydrogen Fluoride. *ACS nano* **9**, 2061–70, doi:[10.1021/nn507277f](https://doi.org/10.1021/nn507277f) (2015).
33. Kanarik, K. J. *et al.* Overview of atomic layer etching in the semiconductor industry. *J. Vac. Sci. Technol. A* **33**, 020802, doi:[10.1116/1.4913379](https://doi.org/10.1116/1.4913379) (2015).
34. Shang, C. K. *et al.* Dry-wet digital etching of Ge_{1-x}Sn_x. *Appl. Phys. Lett.* **108**, 063110, doi:[10.1063/1.4941800](https://doi.org/10.1063/1.4941800) (2016).
35. Gupta, S. & Chen, R. *et al.* Highly Selective Dry Etching of Germanium over Germanium–Tin (Ge_{1-x}Sn_x): A Novel Route for Ge_{1-x}Sn_x Nanostructure Fabrication. *Nano Lett.* **13**, 3783–90, doi:[10.1021/nl4017286](https://doi.org/10.1021/nl4017286) (2013).
36. Li, H. & Chang, C. Characteristics of Sn segregation in Ge/GeSn heterostructures. *Appl. Phys. Lett.* **105**, 151906, doi:[10.1063/1.4898583](https://doi.org/10.1063/1.4898583) (2014).
37. Wang, W. *et al.* Tin surface segregation, desorption, and island formation during post-growth annealing of strained epitaxial Ge_{1-x}Sn_x layer on Ge (001) substrate. *Appl. Surf. Sci.* **321**, 240–244, doi:[10.1016/j.apsusc.2014.10.011](https://doi.org/10.1016/j.apsusc.2014.10.011) (2014).
38. Wang, W. *et al.* Self-assembly of tin wires via phase transformation of heteroepitaxial germanium-tin on germanium substrate. *J. Appl. Phys.* **117**, 225304, doi:[10.1063/1.4922423](https://doi.org/10.1063/1.4922423) (2015).
39. Kato, K. & Taoka, N. *et al.* Formation of high-quality oxide/Ge_{1-x}Sn_x interface with high surface Sn content by controlling Sn migration. *Appl. Phys. Lett.* **105**, 122103, doi:[10.1063/1.4896146](https://doi.org/10.1063/1.4896146) (2014).
40. Zhang, Z. *et al.* Kinetics of Ge diffusion, desorption and pit formation dynamics during annealing of Si_{0.8}Ge_{0.2}/Si (001) virtual substrates. *Phys. Chem. Chem. Phys.* **12**, 7171–83, doi:[10.1039/b927274g](https://doi.org/10.1039/b927274g) (2010).
41. Tanuma, S. *et al.* Calculations of electron inelastic mean free paths. V. Data for 14 organic compounds over the 50–2000 eV range. *Surf. Interface Analysis* **21**, 165–176, doi:[10.1002/\(ISSN\)1096-9918](https://doi.org/10.1002/(ISSN)1096-9918) (1994).
42. Perego, M. & Scarel, G. *et al.* Fabrication of GeO₂ layers using a divalent Ge precursor. *Appl. Phys. Lett.* **90**, 162115, doi:[10.1063/1.2723684](https://doi.org/10.1063/1.2723684) (2007).
43. Patterson, A. L. The Scherrer formula for X-ray particle size determination. *Phys. Rev* **56**, 978–982, doi:[10.1103/PhysRev.56.978](https://doi.org/10.1103/PhysRev.56.978) (1939).
44. LeGoues, F. K. *et al.* Kinetics and mechanism of oxidation of SiGe: dry versus wet oxidation. *Appl. Phys. Lett.* **54**, 644–646, doi:[10.1063/1.100905](https://doi.org/10.1063/1.100905) (1989).
45. Nayak, D. K. & Kamjoo, K. *et al.* Wet oxidation of GeSi strained layers by rapid thermal processing. *Appl. Phys. Lett.* **57**, 369–371, doi:[10.1063/1.103694](https://doi.org/10.1063/1.103694) (1990).
46. Luo, Y. R. Bond Dissociation Energies In CRC Handbook of Chemistry and Physics 2008, Lide, DR, Ed.
47. Deal, B. E. & Grove, A. S. General relationship for the thermal oxidation of silicon. *J. Appl. Phys.* **36**, 3770–3778, doi:[10.1063/1.1713945](https://doi.org/10.1063/1.1713945) (1965).
48. Sung, K. T. & Pang, S. W. Oxidation of silicon in an oxygen plasma generated by a multipolar electron cyclotron resonance source. *J. Vac. Sci. Technol. B* **10**, 2211, doi:[10.1116/1.586191](https://doi.org/10.1116/1.586191) (1992).

49. Kim, K. & An, M. H. *et al.* Oxide growth on silicon (100) in the plasma phase of dry oxygen using an electron cyclotron resonance source. *J. Vac. Sci. Technol. B* **14**, 2667, doi:10.1116/1.589002 (1996).
50. Vrlinic, T., Mille, C., Debarnot, D. & Poncin-Epaillard, F. Oxygen atom density in capacitively coupled RF oxygen plasma. *Vacuum* **83**, 792–796, doi:10.1016/j.vacuum.2008.07.008 (2009).
51. International Technology Roadmap for Semiconductors, 2013. [Online]. Available: <http://www.itrs2.net/>.
52. Ligenza, J. R. Effect of crystal orientation on oxidation rates of silicon in high pressure steam. *J. Phys. Chem.* **65**, 2011–2014, doi:10.1021/j100828a020 (1961).

Acknowledgements

This work was supported by Singapore National Research Foundation through the Competitive Research Program (Grant No: NRF-CRP6-2010-4) and National University of Singapore (R-263-000-B43-733).

Author Contributions

Wei Wang is the main writers and researchers, who provided new ideas and designed investigation plan in research, and wrote the manuscript text and prepared the Figures. Dian Lei performed the EBL. Yuan Dong performed the AFM. Xiao Gong, Eng Soon Tok, and Yee-Chia Yeo help analyze the results.

Additional Information

Competing Interests: The authors declare that they have no competing interests.

Publisher's note: Springer Nature remains neutral with regard to jurisdictional claims in published maps and institutional affiliations.



Open Access This article is licensed under a Creative Commons Attribution 4.0 International License, which permits use, sharing, adaptation, distribution and reproduction in any medium or format, as long as you give appropriate credit to the original author(s) and the source, provide a link to the Creative Commons license, and indicate if changes were made. The images or other third party material in this article are included in the article's Creative Commons license, unless indicated otherwise in a credit line to the material. If material is not included in the article's Creative Commons license and your intended use is not permitted by statutory regulation or exceeds the permitted use, you will need to obtain permission directly from the copyright holder. To view a copy of this license, visit <http://creativecommons.org/licenses/by/4.0/>.

© The Author(s) 2017